Clim. Past Discuss., 10, 1609–1651, 2014
www.clim-past-discuss.net/10/1609/2014/
doi:10.5194/cpd-10-1609-2014

Climate of the Past
Discussions
Open Access

Global sensitivity analysis of Indian Monsoon during the Pleistocene

P. A. Araya-Melo, M. Crucifix, and N. Bounceur

Earth and Life Institute, Georges Lemaître Centre for Earth and Climate Research, Université catholique de Louvain, Louvain, France

Received: 4 March 2014 – Accepted: 18 March 2014 – Published: 11 April 2014

Correspondence to: P. A. Araya-Melo (pablo.arayamelo@uclouvain.be)

Published by Copernicus Publications on behalf of the European Geosciences Union.

Abstract

The sensitivity of Indian Monsoon to the full spectrum of climatic conditions experienced during the Pleistocene is estimated using the climate model HadCM3. The methodology follows a global sensitivity analysis based on the emulator approach of Oakley and O'Hagan (2004) implemented following a three-step strategy: (1) develop an experiment plan, designed to efficiently sample a 5-dimensional input space spanning Pleistocene astronomical configurations (3 parameters), CO_2 concentration and a Northern Hemisphere glaciation index, (2) develop, calibrate and validate an emulator of HadCM3, in order to estimate the response of the Indian Monsoon over the full input space spanned by the experiment design, and (3) estimate and interpret sensitivity diagnostics, including sensitivity measures, in order to synthesize the relative importance of input factors on monsoon dynamics, estimate the phase of the monsoon intensity response with respect to that of insolation, and detect potential non-linear phenomena.

Specifically, we focus on four variables: summer (JJAS) temperature and precipitation over North India, and JJAS sea-surface temperature and mixed-layer depth over the north-western side of the Indian ocean. It is shown that precession controls the response of four variables: continental temperature in phase with June to July insolation, high glaciation favouring a late-phase response, sea-surface temperature in phase with May insolation, and continental precipitation in phase with July insolation, and mixed-layer depth in antiphase with the latter. CO_2 variations controls temperature variance with an amplitude similar to that of precession. The effect of glaciation is dominated by the albedo forcing, and its effect on precipitation competes with that of precession. Obliquity is a secondary effect, negligible on most variables except sea-surface temperature. It is also shown that orography forcing reduces the glacial cooling, and even has a positive effect on precipitation.

As regards the general methodology, it is shown that the emulator provides a powerful approach, not only to express model sensitivity, but also to estimate internal

CPD
10, 1609–1651, 2014

variability (based on the nugget term introduced in the correlation function of the emulator) and detect anomalous simulations.

1 Introduction

Palæoclimate observations and simulations with climate models consistently show a response of the Indian Monsoon to climate and forcing changes associated with glacial–interglacial cycles. In particular, many authors have used general-circulation-model (GCM) simulations to study the sensitivity of Indian Monsoon to changes in astronomical parameters (e.g. Kutzbach and Street-Perrott, 1985; Kutzbach and Guetter, 1986; Prell and Kutzbach, 1987; Anderson et al., 1988; Kutzbach and Liu, 1997; Braconnot et al., 2002, 2008; Braconnot and Marti, 2003).

Namely, early experiments used atmospheric GCMs and required prescribing sea-surface temperatures. Kutzbach and Street-Perrott (1985) (see also Kutzbach and Guetter, 1986) used the NCAR climate model to provide 2 sets of 7 experiments spanning the last 18 000 years, assuming perpetual January and July conditions, respectively. These simulations showed that changes on the season of perihelion affect significantly Earth's climate. Specifically, at 18 kyr BP, simulations showed cooler tropics than at present, but most regions had similar rainfall to present levels or were slightly drier. The simulations showed a major strengthening of northern monsoons between 12 and 6 kyr BP, associated with the enhanced seasonal radiation contast. The effect was opposite in the southern tropics: the changed insolation produced decreased seasonality and less intense summer rains in tropical southern parts of the continents. These simulations were further analysed and extensively compared with palaeoclimate evidence in the framework of the Cooperative Holocene Mapping Project, *COHMAP* (Anderson et al., 1988; Kutzbach and Ruddiman, 1993). Prell and Kutzbach (1987) also performed a series of 13 GCM simulations accounting for changes in orbital parameters, CO_2 concentration and sea-level over the last 150 000 years, and confirmed the important effect of precession on tropical monsoons.

CPD
10, 1609–1651, 2014

Still based on atmosphere-only models, Dong and Valdes (1998) documented a negative relationship between South Eurasian snow mass and the amount of precipitation over India, and Masson et al. (2000) showed that high insolation can generate increased monsoon activity, even with glacial boundary conditions.

Felzer et al. (1998) also performed a series of simulations to study the sensitivity of late-Quaternary climates to ice sheets, orbital insolation and CO_2, with sea-surface temperature (SST) computed with a slab ocean. Consistenly with the earlier findings of Kutzbach and Street-Perrott (1985) and Anderson et al. (1988), they found that, at 21 kyr BP, weaker glacial monsoons are the result of both lower CO_2 concentrations and the large Last Glacial Maximum ice sheets. At 14 and 11 kyr BP, the astronomical forcing dominates the monsoon response, which is maximum around 11–9 kyr BP.

Kutzbach and Liu (1997) provide an early application of ocean–atmosphere models to palaeoclimate studies, based on an asynchronous coupling procedure. Again, the increase in the seasonal cycle insolation in the Northern Hemisphere increased the sea surface temperature in the tropical Atlantic 6000 years ago in late summer, which in turn further enhanced the summer monsoon precipitation in northern Africa by more than 25 %, compared to simulations with prescribed, pre-industrial sea-surface temperatures.

Braconnot and Marti (2003) used a fully coupled ocean–atmosphere model, and specifically focused on Indian monsoon and its effect on Indian and South-East Asia climatology. They presented three experiments specifically chosen to study the sensitivity of the seasonality of the monsoon signal to the time at which perihelion is reached. Namely, an "early-phase" configuration (perihelion reached in April) produces a stronger monsoon, which occurs earlier in the year than a "late-phase" configuration (perihelion reached in September).

Intercomparison exercices, based on experiments with different climate models, allowed to further test the dependency of these conclusions to model choice. Specifically, Joussaume et al. (1999) and Braconnot et al. (2002) investigated the enhancing of the summer monsoon in the Northern Hemisphere at 6 kyr BP based

CPD
10, 1609–1651, 2014

on a set of 17 atmosphere-only simulations, as part of the Paleoclimate Modeling Intercomparison Project (PMIP). It was found that in all simulations, the 6 kyr BP orbital configuration resulted in a continental warming over the Eurasian continent, which enhances the Indian Monsoon. They also found that the changes in monsoon precipitation depends on the magnitude of the continental warming. Later, Braconnot et al. (2008), using seven ocean–atmosphere couple simulation models, compared the monsoon response to orbital parameters changes between the Eemian and Holocene period. Their study confirmed the strong relationship between increased seasonality of insolation in the Northern Hemisphere and monsoon amplification.

It is thus clear that astronomical forcing (eccentricity, longitude of perihelion, and obliquity), CO_2 and ice boundary conditions determine the history of monsoon dynamics. One general difficulty is to disentangle the individial and combined effects of these five factors influences at reasonable computing cost. A classical factorial experiment, with only 2 distinct levels per factor (a minimum and a maximum range) would already require 32 experiments. Three levels would require 243 experiments.

Fortunately, the theory of experiment design and global sensitivity analysis with computer models provides us with strategies to address this problem. The method featured here follows Oakley and O'Hagan (2004), who further refer to the earlier contributions of Sacks et al. (1989) and Homma and Saltelli (1996). The principle rests on the combination of an adequate experiment design with a statistical model. The purpose of the latter is to interpolate the GCMs outputs in order to produce appropriate numerical and visual diagnostics.

The statistical model, hence, act as a fast surrogate of the GCMs, and for this reason it is commonly named "emulator" in the literature (O'Hagan, 2006). Specifically, the term emulator refers to the following properties (O'Hagan, 2006; Petropoulos et al., 2009):

- it is derived from a small number of model runs filling the entire multidimensional input space,

CPD
10, 1609–1651, 2014

– once the emulator is built, it is not necessary to perform any additional runs with the model.

The objective of the present study is to develop a first experience in the application of the emulator framework for a sensitivity analysis of palaeoclimates relevant for the entire period of the Pleistocene. More specifically, we address the sensitivity of the Indian Monsoon to the three components of the astronomical forcing, plus carbon dioxide concentration and ice boundary conditions.

To this end, an ensemble of 61 simulations with varying input parameters are run with the climate model HadCM3 Gordon et al. (2000). The climate analysis is inspired from the earlier work of Zhao et al. (2005), and emphasis is set on benefits of the emulator framework for understanding the monsoon response.

The paper is structured as follows. Section 2 provides a brief description of the emulator and the simulations used. Section 3 details the results of applying the emulator to the Indian monsoon region, focusing on the relations of the parameters under study and their impact in the climate of the monsoon. We also study the specific influence of ice sheet topographic forcing. The conclusion follows in Sect. 4.

2 Methodology

2.1 Experiment design

Five inputs factors are considered here: the three elements of astronomical forcing (eccentricity e, longitude of perihelion ϖ and obliquity ε), the concentration in carbon dioxide (CO_2), and a variable called the ice or glaciation level, which combines ice and orography forcings associated with the presence of continental ice in the Northern Hemisphere.

The three elements of astronomical forcing are combined under the form of $e\sin\varpi$, $e\cos\varpi$ and obliquity ε. This choice is justified by the fact that these combinations produce orthogonal patterns in the season–latitude space, and generally insolation at any point and time in year is well-approximated as a linear combination of those terms (Loutre, 1993). The factors $e \sin \varpi$ and $e \cos \varpi$ are sampled in the range $[-0.05, 0.05]$, while ε is varied in the range 22–25°. On the other hand, CO_2 is sampled in the range 180–280 ppm.

The glaciation level is determined as follows. Our purpose is to select 11 realistic boundary conditions representative of glacial–interglacial dynamics. Pragmatically, we sampled these boundary conditions among the series prepared by Singarayer and Valdes (2010), and supplied to us by Paul Valdes. Level 1 corresponds to present-day conditions, and levels 2 to 11 are chosen such as to represent approximately ten equally spaced top altitudes of the North American ice sheet, within the glaciation phase. One limitation of this design for the present purpose is that levels 3 to 11 effectively represent similar ice sheet areas – thus similar albedo forcing – even though they sample very different ice sheet volume (see Fig. 3).

The next step is to effectively select the input factors combinations used in the simulation ensemble. Theoretical considerations and experience point to the latin hypercube design (McKay et al., 1979; Morris and Mitchell, 1995; Urban and Fricker, 2010) as a good starting point for computer experiments. The principle, for a latin hypercube design of n elements, is to divide the ranges covered by each input factor into n distinct categories, each experiment sampling one of the n categories without replacement. We followed the standard practice of associating the latin hypercube design with additional constraints (Joseph and Hung, 2008, e.g.): namely, maximize the minimum distance between every two pair of points (specifically, the Euclidean distance in the normalized input space), and maximize the covariance matrix of the design, again expressed in the normalized input space. By maximizing the distance between points we ensure the experimental design to be space filling.

In the present context, two additional constraints need to be accounted for in order to avoid sampling unrealistic inputs that would be uninformative for the sensitivity analysis of climate over the Pleistocene: exclude forcings with $e > 0.05$, and exclude combinations of high CO_2 and high glaciation levels (and conversely), delineated by an

CPD
10, 1609–1651, 2014

ellipse with great and small axes as shown on Fig. 1. To satisfy these constraints, the design points generated by the latin hypercube sampling procedure and lying in the exclusion zone are geometrically projected on the allowed region. This procedure may break some of the original properties of the design (maxi–min and orthogonality), but it offers the practical advantage of enhancing the coverage of the input space near its boundary.

Note that this design is in principle suitable for continuous factor ranges only. The glaciation level used for experiments is an integer obtained by rounding the value obtained by this process to the closest integer. Designs specifically adapted for input spaces mixing categorical and continuous variables could best be implemented in the future (see, e.g., MacCalman, 2013, for an up-to-date review).

Table 1 lists the simulations with their input parameters. The choice of 61 members is a conservative implementation of the recommendation of 10 experiments per input factors (Loeppky et al., 2009). In fact, a first 57 member design was produced using the method above, to which 4 members were added (exp. 20–23). These experiments are idealised orbital changes that were performed during the first phase of this project in order to explore locally the model sensitivity to astronomical forcing.

2.2 Climate simulator

The climate model – referred to in this context as the simulator – is the General Circulation Model HadCM3 (Gordon et al., 2000), associated with the MOSES2 surface component (Essery et al., 2003).

The atmospheric component dynamics and physics are resolved on a $3.75^\circ \times 2.5^\circ$ longitude–latitude grid. On the other hand, the oceanic component has a horizontal resolution of $1.25^\circ \times 1.25^\circ$.

Initial conditions are the final state of the PMIP2 0K experiment featured in Braconnot et al. (2007). Each simulation is run for 400 years, except for the *xadk#* set. Accidentally, the first 200 years did not account for ice sheet topography. This was corrected for the following 200 years. In the case of the *xadk#* simulations, they were

CPD
10, 1609–1651, 2014

ran 300 years, accounting for ice sheet topography from the beginning. Typical residual deep-ocean temperature trends are of the order of 10^{-4} °C year^{-1}.

The last 100 years of all simulations with orographic forcing were retained for analysis. Over this interval, the top-of-the-atmosphere imbalance ranges between −0.2 and −0.1 W m^{-2}. The last 100 years of the experiments section without orographic forcing are also used for an investigation of the specific effect of the orographic forcing (cf. Sect. 3.6).

2.3 Emulator

The emulator is a statistical model calibrated on the simulator output. Its role is to predict simulator outputs for untried experiments. We follow here the Gaussian process framework of Sacks et al. (1989), Kennedy and O'Hagan (2000) and Oakley and O'Hagan (2002).

Let $\boldsymbol{x}_j$ be the input vector associated with the jth component of the experiment design. The output of the climate model is modeled as a stochastic process combining a global response function (the regressors) with a local component. It is fully specified by the mean m and a covariance V function. They have the following priors:

$$m(\boldsymbol{x}) = \boldsymbol{h}'(\boldsymbol{x})\beta \tag{1}$$

$$V(\boldsymbol{x},\boldsymbol{x}^\star) = \sigma^2[c(\boldsymbol{x},\boldsymbol{x}^\star)] \tag{2}$$

where $c(\boldsymbol{x},\boldsymbol{x}^\star)$ is the Gaussian process correlation function, σ^2 its variance, $\boldsymbol{h}(\boldsymbol{x})$ is a $(q\times 1)$ vector of a priori known regression functions and β is the vector of corresponding regression coefficients. Note that the $()'$ is used to denote a horizontal vector.

Let $\boldsymbol{y}$ be the vector of actual outputs, obtained by running the model at the n design points. The posterior estimate of the simulator output at any input point $\boldsymbol{x}$ is given by

CPD
10, 1609–1651, 2014

the following expressions (Oakley and O'Hagan, 2002):

$$m(\boldsymbol{x})|\boldsymbol{y} = \boldsymbol{h}'(\boldsymbol{x})\beta + \boldsymbol{T}(\boldsymbol{x})\mathbf{A}^{-1}(\boldsymbol{y} - \mathbf{H}\hat{\beta})$$
$$V(\boldsymbol{x},\boldsymbol{x}^\star)|\boldsymbol{y} = \hat{\sigma}^2[c(\boldsymbol{x},\boldsymbol{x}^\star) - \boldsymbol{T}(\boldsymbol{x}^\star)\mathbf{A}^{-1}\boldsymbol{T}'(\boldsymbol{x}) + P(\boldsymbol{x})(\mathbf{H}^\mathrm{T}\mathbf{A}^{-1}\mathbf{H})^{-1}\boldsymbol{P}'(\boldsymbol{x}^\star),$$

where

$$\hat{\sigma}^2 = \frac{1}{n-q-2}(\boldsymbol{y} - \mathbf{H}\hat{\beta})^\mathrm{T}\mathbf{A}^{-1}(\boldsymbol{y} - \mathbf{H}\hat{\beta})$$
$$\hat{\beta} = (\mathbf{H}^\mathrm{T}\mathbf{A}^{-1}\mathbf{H})^{-1}\mathbf{H}^\mathrm{T}\mathbf{A}^{-1}\boldsymbol{y} \tag{3}$$

The operator $()^\mathrm{T}$ is the matrix transpose, $\boldsymbol{T}(\boldsymbol{x})_j = c(\boldsymbol{x},\boldsymbol{x}_j)$, $\mathbf{A}_{i,j} = c(\boldsymbol{x}_i,\boldsymbol{x}_j)$, $\mathbf{H}$ the design point regression matrix, the jth row of which is $\boldsymbol{h}'(\boldsymbol{x}_j)$ and finally $P(\boldsymbol{x}) = \boldsymbol{h}'(\boldsymbol{x}) - \boldsymbol{T}(\boldsymbol{x})\mathbf{A}^{-1}\mathbf{H}$.

The above expressions assume the vague prior $(\boldsymbol{\beta},\sigma^2) \propto \sigma^{-2}$ proposed by Berger et al. (2001) and used by, e.g., Oakley and O'Hagan (2002) and Bastos and O'Hagan (2009). Note that with this prior the posterior state distribution is a student-t distribution with $n-q$ degrees of freedom, but it is close enough to being Gaussian to be considered as such in the following discussion.

With this framework, the choices of the regression functions $\boldsymbol{h}(\boldsymbol{x})$ and the Gaussian process correlation function c are application dependent. This is where the user has the opportunity to inject knowledge on the expected response of the simulator.

For this application, linear regression is an adequate choice because the seasonal and annual forcings are almost linear with the input factors, except possibly for glaciation level. Hence, $\boldsymbol{h}'(\boldsymbol{x}) = (1,\boldsymbol{x}')$. The correlation function c is the exponential decay with nugget, discussed in length in Andrianakis and Challenor (2012):

$$c(\boldsymbol{x},\boldsymbol{x}^\star) = \exp[-(\boldsymbol{x}'\Lambda^{-2}\boldsymbol{x}^\star)] + \nu\delta(\boldsymbol{x},\boldsymbol{x}^\star), \tag{4}$$

where $\delta(\boldsymbol{x},\boldsymbol{x}^\star)$ is 0 except where $\boldsymbol{x} = \boldsymbol{x}^\star$, and Λ is a scaling matrix, chosen to be diagonal with components λ_i. The term involving the nugget ν can be justified as a regularization *antsatz* to circumvent poor matrix conditioning (Pepelyshev, 2010) and mis-specification of the correlation function Gramacy and Lee (2012). In the present context it also has a more directly interpretable function. Indeed, the output of HadCM3 depends to some degree on a number of factors not explicitly accounted for here, namely initial conditions, experiment length and averaging time span. The effects of these non-explicit inputs can be absorbed by the nugget.

Following Kennedy and O'Hagan (2000), hyperparameters are obtained by maximising the emulator likelihood (the expression used here is from Andrianakis and Challenor, 2012):

$$\log L(\nu, \Lambda) = -\frac{1}{2}\left(\log\left(|\mathbf{A}||\mathbf{H}^{\mathrm{T}}\mathbf{A}^{-1}\mathbf{H}|\right) + (n-q)\log(\hat{\sigma}^2)\right)$$

More specifically, Andrianakis and Challenor (2012) recommend the use of a *penalised likelihood*, that imposes a restriction on the amplitude of the nugget:

$$\log L^{\mathrm{p}}(\nu, \Lambda) = \log L(\nu, \Lambda) - 2\frac{\overline{M}(\nu, \Lambda)}{\epsilon \overline{M}(\infty)} \tag{5}$$

where $\overline{M}(\nu, \Lambda)$ is the Mean Squared Error between the training points and the emulator's posterior mean at the design points, and $\overline{M}(\infty)$ is its asymptotic value at $\lambda_i \to \infty$. We use $\epsilon = 1$.

2.4 Sensitivity measures

One of the early applications of Bayesian approach for emulators was to estimate sensitivity measures that quantify the influence of a factor on the simulator output (Oakley and O'Hagan, 2004). Although originally developed to estimate uncertainties associated with uncertain inputs, the indices may be reinterpreted as indicators of variance generated by known variations in inputs. Call $\rho(\boldsymbol{x})$, the time-wise occupation density of the input space. This occupation density along the components of the

CPD
10, 1609–1651, 2014

astronomical forcing can be estimated with histograms of long time series generated with known astronomical solutions, such as Berger (1978) For CO_2 and glaciation level we consider the following empirical distribution to broadly capture the observed covariance between CO_2 and glaciation level:

$$\rho(c^\star,i^\star) \propto \begin{cases} \mathcal{N}\left(0.5, \frac{3}{8}\begin{pmatrix} 1 & \frac{1}{3} \\ -1 & \frac{1}{3} \end{pmatrix}^2\right) & \text{where } 0 < c^\star < 1, \quad 0 < i^\star < 1 \\ 0 & \text{elsewhere} \end{cases} \tag{6}$$

where $c^\star, i^\star$ are inputs standardised as follows:

$$c^\star = (CO_2 - 180\,\text{ppm})/(100\,\text{ppm}) \tag{7}$$

$$i^\star = (\text{glaciation level} - 1)/10 \tag{8}$$

With this density at hand, it is now possible to estimate, for each factor (or combination thereof) a *mean* and a *variance* (Oakley and O'Hagan, 2004).

Define the function $m_p(\boldsymbol{x}_p)$, where p refer to one or several components of $\boldsymbol{x}$, as the expected mean of $\boldsymbol{x}$ given $\boldsymbol{x}_p$ fixed, and obtained by integrating the emulator over the sub-space $\chi_{\overline{p}}$ covered by the remaining components:

$$m_p(\boldsymbol{x}_p) = \frac{1}{\rho_p(\boldsymbol{x}_p)} \int\limits_{\chi_{\overline{p}}} m(\boldsymbol{x}|\boldsymbol{x}_p)\rho(\boldsymbol{x}|\boldsymbol{x}_p)\,\mathrm{d}\boldsymbol{x}, \quad \text{where} \quad \rho_p(\boldsymbol{x}_p) = \int\limits_{\chi_{\overline{p}}} \rho(\boldsymbol{x}|\boldsymbol{x}_p). \tag{9}$$

The conditional dependency on $\boldsymbol{y}$ introduced in Eq. (3) is dropped for readability. The notation $\boldsymbol{x}|\boldsymbol{x}_p$ means that the integral is made over all the remaining components of $\boldsymbol{x}$ with given $\boldsymbol{x}_p$.

The expected *covariance* of the Gaussian process given $\boldsymbol{x}_p$ is given by a double integral:

$$V_{pp}(\boldsymbol{x}_p, \boldsymbol{x}_p^\star) = \frac{1}{\rho_p(\boldsymbol{x}_p)\rho_p(\boldsymbol{x}_p^\star)} \int \int\limits_{\chi_{\overline{p}} \times \chi_{\overline{p}}} V(\boldsymbol{x}_1|\boldsymbol{x}_p, \boldsymbol{x}_2|\boldsymbol{x}_p^\star)\mathrm{d}\rho(\boldsymbol{x}_1|\boldsymbol{x}_p)\mathrm{d}\rho(\boldsymbol{x}_2|\boldsymbol{x}_p^\star) \tag{10}$$

CPD
10, 1609–1651, 2014

This quantity may further be integrated over the possible values of $\boldsymbol{x}_p$:

$$\Sigma_p = \int_{\chi_p} \left[m_p(\boldsymbol{x}_p)^2 + V_{pp}(\boldsymbol{x}_p, \boldsymbol{x}_p) \right] \mathrm{d}\rho_p(\boldsymbol{x}_p) \tag{11}$$

where χ_p is the domain sub-space covered by factor p. Define, consistently,

$$\Sigma_0 = \left[m_0^2 + V_{00} \right], \tag{12}$$

where the notation m_0, V_{00} implies that the space $\chi_{\overline{p}}$ that appears in Eqs. (9) and (10) is the whole input domain χ, and, finally,

$$\Sigma = \int_{\chi} \left[m(\boldsymbol{x})^2 + V(\boldsymbol{x}, \boldsymbol{x}) \right] \mathrm{d}\rho(\boldsymbol{x}). \tag{13}$$

Then, the emulator output variance associated with input factor(s) p may be measured either as

- $S_p = \Sigma_p - \Sigma_0$: this is the expected loss in output variance that would occur if factor p was fixed, all other factors varying, or
- $\overline{S}_p = \Sigma - \Sigma_{\overline{p}}$: this is the expected output variance obtained by varying factor p, all other factors fixed.

The distinction is especially important when $\rho(\boldsymbol{x}|\boldsymbol{x}_p)$ depends on x_p. Indeed, in this case the variance of the mean effect includes both a contribution from the isolated effect of the factor on the simulator output, and an implicit effect associated with the changes in the probability distribution of other factors associated with a change in $\boldsymbol{x}_p$.

The variance $\overline{S}_p$ discards the second effect. It is therefore a better starting point to explore physical mechanisms. Following Homma and Saltelli (1996) (see also Chapter 1 of Saltelli et al., 2004), we use this measure here.

CPD
10, 1609–1651, 2014
Sensitivity analysis of Asian Monsoon
P. A. Araya-Melo et al.

Note, finally, that $\overline{S}_p$ may be further split into $\overline{S}_p^m + \overline{S}_p^V$, i.e., one can separate the contributions from m and V appearing in Eqs. (11)–(13). $\overline{S}_p^m$ is the output variance induced by expected changes of simulator output in response to changes in input p. This is thus the quantity of physical interest. $\overline{S}_p^V$ is an effect produced by the emulator variance, i.e., the uncertainty associated with using an emulator rather than the simulator. Hence, $\overline{S}_p^m$ should only be considered to be significant if it is large enough compared to $\overline{S}_p^V$.

3 Results

In order to study the Indian Monsoon, we define two regions: Northern India (NI), with coordinates 70–100° E, 20–40° N, and northwestern Indian Ocean (IND), with coordinates 55–75° E, 5–15° N, (see Zhao et al., 2005). The chosen regions are depicted in Fig. 2, in which the sea-level pressure and surface temperature of one of the simulations are shown. The NI region covers the Indian continent and part of the Himalayas (which is dry today), while IND covers the northwestern part of the Indian Ocean.

We focus specifically on four physical variables representative of the Summer Indian Monsoon process: June-July-August-September (JJAS) temperature and precipitation on the continental box, and JJAS sea surface temperature (SST) and mixed-layer depth on the Indian Ocean box. Over the experiment design, continental temperature varies between 15 and 21 °C. Precipitation varies between 72 and 230 mm month^{-1}, SST between 25 and 31 °C, and mixed-layer depth between 29 and 59 m. For emulation, the logarithms of precipitation and mixed-layer depth are used, because the distributions of the latter are more Gaussian than those of the absolute values.

3.1 Emulation validation

An emulator using all 61 experiments is calibrated using the procedure given in Sect. 2.3, with scales λ_i (with $i = 1, ..., 5$) and nugget determined by maximization of the penalised likelihood. The performance of the emulator is then assessed following a leave-one-out cross validation approach, that is, constructing 60 emulators to predict the experiment being left out. Figure 4 shows the result of this leave-one-out cross validation procedure for SST and mixed-layer depth only, the other variables being discussed later.

This leads us to the following observations:

1. the optimal covariance scales are generally commensurate with the range covered by the input factors. This is the ideal scenario, as it implies that the stochastic component of the Gaussian process is smooth, and may thus be suitably calibrated by the experiment design.

2. There are however some instances where the optimum covariance scales are much greater than the scale of the variables: this is observed on all output variables for the response in CO_2, and, to a lesser extent, for obliquity. A large covariance scale implies that response is linear with respect to the factor, which is indeed a realistic outcome for CO_2, in the range considered. This is not a problem on its own. It simply informs the user that a sparser sampling of this factor would have worked as well.

3. The leave-one-out cross validation plot reveals two outliers for SST (experiments 11 and 40) and one outlier for mixed layer (experiment 40). We term "outliers" experiments generating output that is predicted with an error of more than 3 standard deviations when they are left out of the calibration procedure. The signature of these outliers is also visible on the mean effect plots (Fig. 6). These plots, which will be commented on more in depth in Sect. 3.5, represent the mean effect such as given by Eq. (9), here as a function of glaciation level and $e \sin \varpi$,

and assuming CO_2 fixed. The figure reveals convoluted contours, most notably the 26.25 and 26.5 °C isotherms on the SST plot and the 38.5 m iso-depth that conflict with our expectation of a smooth response structure.

Further inspection of the outliers reveals a clear warm/cold/warm pattern in the North Atlantic, and cooling over the rest of the ocean, exemplified here by comparing experiments 11 and 15 (Fig. 11). This pattern has been seen before in HadCM3, most notably in early experiments of the Last Glacial Maximum (Hewitt, 2003). It was associated with an enhancement of the North Atlantic Overturning circulation cell, and can be annealed by addition of freshwater in the North Atlantic (Hewitt et al., 2006). Experiments 11 and 40 have, however, low to moderate glaciation levels. Hence, the most reasonable explanation seems that the 100 year sampling procedure has picked up some rarely visited ocean circulation regime that affects the climate system globally. Although this regime may be of relevance for palæoclimate analysis, it appeared here sufficiently anomalous to be considered off our focus. Consequently, the emulator was recalibrated using the remaining 59 experiments.

This new emulator with new scales λ_i and nugget (see Table 2) then presents quite convincing validation scores (Fig. 5):

1. all emulators capture between 38 (mixed-layer) and 43 (continental temperature) of the left-one-out experiments within 1 standard deviation, and between 56 and 58 within 2 standard deviations, which roughly correspond to the 66 and 95 % ratios expected for a normal distribution;

2. the errors normalised by standard deviation are compatible with a normal distribution based on the Shapiro–Wilk normality test, except for continental temperature ($p = 0.03$);

3. there is no error exceeding 3 standard deviations.

4. Finally, the suspicious anomalies generated on the glaciation/precession plots are cleared (Fig. 13).

CPD
10, 1609–1651, 2014
Sensitivity analysis of Asian Monsoon
P. A. Araya-Melo et al.

In addition, the nugget value obtained by maximizing the likelihood is overall consistent with what we know from the model variability. The nugget quantifies the uncertainty of the "observation", here related to the specific choice of one 100 year simulation sample as representative of the model mean stationary state. The residual error in the emulator is of the order of $\hat{\sigma}^2 \nu$, but it can be estimated precisely by looking at the posterior variance at design points. Here, the obtained nuggets induce residual uncertainties with standard deviations of 0.04 °C on continental temperature, 2.3 % on precipitation, 0.05 °C on SST, and 0.7 % on mixed-layer depth. All these values are consistent with the 100 year variances of the corresponding quantities in HadCM3.

Thus, the emulator calibration procedure has been able to infer information on model variability from an ensemble of simulation outputs that are all 100 years averages. This is quite remarkable.

3.2 Sensitivity indices

Figure 7 summarizes the sensitivities of the four different variables to the external factors. $e \cos \varpi$ and $e \sin \varpi$ are grouped together under the term "precess", for climatic precession. Two bars are shown for every factor, quantifying the sensitivities Σ^m (grey) and Σ^v (black). Remember that we want to focus our attention on factors for which Σ^m is much larger than Σ^v.

Specifically, continental summer temperature is primarily determined by precession, CO_2 and, to a lesser extent, ice volume. It shows no significant sensitivity to obliquity. Continental precipitation is also mainly driven by precession and less to ice volume. Contrarily to temperature, it exhibits no sensitivity to CO_2.

Similar to continental temperature, SST is primarily driven by precession and CO_2 and, to a lesser extent, ice volume. It also shows a larger response to obliquity. Finally, mixed-layer depth shows a pattern similar to precipitation, except that the response to obliquity is not significant compared to the sources of uncertainty induced by the emulation and sampling variance.

CPD
10, 1609–1651, 2014

3.3 Sensitivity to precession

Figure 12 displays the effects of precession on the four variables retained for analysis. The choice here is to show the effects by fixing ice and CO_2 concentration at three distinct levels representative of the course of glaciation (from top to bottom): glaciation level 1/CO_2 = 280 ppm, glaciation level 5/CO_2 = 230 ppm and glaciation level 11/CO_2 = 180 ppm. Quantities are further averaged over obliquity. In order to ease the interpretation, the months representing the time at which perihelion is reached are written on the plots: June for $\varpi = 90^{\circ}$, September for $\varpi = 180^{\circ}$ etc. That is, neglecting slow transient effects that could be associated with the deep ocean response, this graphical representation provides an indication of the phase lag between the climate response and the precession forcing of insolation.

Specifically, the temperature response is in phase with June insolation at low glaciation levels, and in phase with July insolation at mid- and high-glaciation stages. In addition, the low-glaciation response to precession shows a marked asymmetric pattern, with temperatures at June perihelion that are lower than a linear extrapolation would have predicted.

This feature may physically be understood by considering the summer precipitation response. Precipitation enhances latent heat cooling when perihelion is around July. This effect gradually weakens as glaciation takes place and the total amount of precipitation declines, hence the drift towards a more linear response. At higher glaciation levels the JJAS temperature response phase also aligns with July insolation.

The maximum precipitation is obtained when perihelion is reached in early July. Among the series of experiments shown by Braconnot et al. (2008), this is indeed the 126 000 yr BP experiment (i.e., July perihelion) experiment that shows the strongest precipitation response over India.

Furthermore, continental precipitation and mixed-layer show opposite response phases to precession. This result is consistent with the earlier findings of Zhao et al. (2005), who identified a shoaling of the mixed-layer in this region by

CPD
10, 1609–1651, 2014

about 6 m, consistent across different models, in 6000 yr experiments (September perihelion). Braconnot and Marti (2003) examined also two nearly-opposite precession configurations with the IPSL model, corresponding to perihelion in April and October, respectively, and they found a shoaling of the mixed-layer compared to the present-day (perihelion in January) in both cases.

Zhao et al. (2005) attributed the mixed-layer shoaling to a stratification effect involving the response of SST. On this point, our analysis reveals that the maximum SST response occurs when perihelion is reached in May. This is not so surprising given that the ocean thermal inertia generally imposes a lag of a few months between the forcing and the response. This response, however, induces an asymmetry between perihelion in April and perihelion in October, the first one only showing anomalously high SSTs. This is consistent with the analysis of seasonal cycle response provided by Braconnot and Marti (2003).

3.4 Sensitivity to obliquity

The response of obliquity is mostly linear. The range of obliquity covered during the Pleistocene induces negligible continental temperature response over the West-Indian box. It also induces a slight increase in precipitation. Regarding the Indian Ocean box, there is a somewhat larger effect on SST compared to continental temperature, but not significant. As for the mixed-layer depth, the response to obliquity is negligible.

In order to better understand obliquity effect, we considered the four *ideal cases* experiments (simulations 20–23, see Table 1). Specifically, we discuss here experiments 22 and 23, termed OBL23 and OBL24. They use zero eccentricity, same CO_2 concentration and glaciation level, and differ by the configuration of obliquity (24 and 23°, respectively). The temperature difference map, for JJAS, reveals the signature of obliquity-induced insolation changes, with a warming of Northern Hemisphere continent, and slight cooling of significant areas of the tropical oceans (see Fig. 9)

CPD
10, 1609–1651, 2014

P. A. Araya-Melo et al.

3.5 Sensitivity to CO_2 and glaciation level

The response of all variables to CO_2 is best captured by linear processes (optimal λ_i largely exceeds the range covered by the experiment design). Hence, the contribution of CO_2 to the climate response may be estimated straightforwardly from the coefficients $\hat{\beta}$, given by Eq. (3). Namely, the continental temperature and SST responses to the 100 ppm range covered by the experiment design are 2.03 and 1.40 °C, respectively. This corresponds to CO_2 doubling sensitivities of 3.20 and 2.21 °C, in line with the reported HadCM3 sensitivity in CO_2 doubling experiments (see., e.g., Fig. 5 of Williams et al., 2001) The responses of precipitation and mixed-layer are, again, opposite and very moderate: +6 % of precipitation over 100 ppm and – 0.5 % of mixed-layer depth.

Figure 8 shows the response of continental temperature (left panel), sea surface temperature (middle panel) and mixed-layer depth (right panel) to the variations of CO_2 concentration and glaciation level. The temperature ranges covered by CO_2 and glaciation levels are of the order of 1 and 2 °C for the continent and ocean surface, respectively. The continental ice effect is mainly present between glaciation levels 1 and 3. With the ice sheet reconstructions used here, the ice area extent responsible for the shortwave forcing reaches almost its maximum value at glaciation level 3. Further increasing the glaciation levels affects climate predominantly through the orography forcing (cf. Sect. 3.6).

Interestingly, the figure shows that SST is insensitive to glaciation level. However, Fig. 7 shows a dependency on it. What happens is that the signal is reverse for low and high glaciation levels. When integrating over obliquity, these signals are averaged, so that dependency on glaciation is masked.

3.6 Orographic effect

Finally, we consider the differences between the simulations with and without orography forcing of the ice sheets. The latter is potentially important given that mountains and elevated land masses affect the atmospheric circulation and precipitation patterns, and

CPD
10, 1609–1651, 2014

then the whole climate system. To this end, an emulator was calibrated on the available present-day orography experiments.

The net effect orography can then be seen in Fig. 10, where all four variables are plotted as a function of the glaciation level. Black solid lines show the respective variables obtained with the standard experiment design, while red solid lines show the response obtained with the experiment design assuming pre-industrial orography, regardless of the presence of ice sheets. The value plotted is obtained from Eq. (9). Note that by construction this value is also implicitly a function of CO_2 concentration, which enters Eq. (9) via the factor $\rho(\boldsymbol{x}|\boldsymbol{x}_{\mathrm{ice}})$. Dotted lines indicates a 1-σ deviation, in both cases, based on Eq. (10), using $\boldsymbol{x}_p = \boldsymbol{x}_p^{\star}$.

A clear deviation is seen around glaciation level 3. This effect is due to the fact that, as explained in Sect. 2.1, levels 3–11 represent effectively similar ice sheet area, but significantly higher orography (see Fig. 3). Hence, the albedo forcing dominates over the lower range of glaciation levels (1–3), with decreasing temperatures, precipitation and mixed-layer shoaling. The orography–no orography differences appear more markedly above indice 3: orography reduces the cooling trends, by as much as 1 °C on the continent at glaciation level 11, and even reverses the precipitation trend. It is known that ice orography forcing may impact monsoon precipitation regimes (Prell and Kutzbach, 1997; Yin et al., 2009), though to our knowledge the specific effect of Northern Hemisphere ice sheet orography on Indian monsoon is yet to be documented. The warming signal caused by orography may be understood by considering the increase in surface potential temperature over elevated regions, similar to what is seen today over the Tibetan Plateau. Because of these high potential temperature, down-sloping air is effectively warmer than it would be in absence of orography forcing, and contributes here to increase the Northern Hemisphere continental surface temperature. Orographic forcing generally induces atmospheric circulation anomalies and effects on ocean circulation and stratification. Namely Fig. 10 suggests a weak positive effect on mixed-layer depth, though quite small compared the astronomical forcing effects. An in-depth analysis of these effects falls beyond the scope of the present contribution.

CPD
10, 1609–1651, 2014

4 Conclusions

We performed a global sensitivity analysis of the climate response of the Indian Monsoon to the astronomical forcing ($e\sin(\varpi)$, $e\cos(\varpi)$, ε), CO_2 concentration and glaciation level.

To achieve this, we make use of an *emulator*, that is, a statistical model calibrated on the outputs of a set of well-chosen experiments, in order to explore and quantify globally the sensitivity of the model to each parameter and combinations thereof.

The present study focuses on four variables: continental temperature, continental precipitation, sea surface temperature and mixed-layer depth. These variables were averaged for the JJAS season over northern India and northwestern Indian Ocean.

The method is divided in three steps:

- *Design an experiment plan.* We adopted a latin-hypercube design, optimised following two constraints: maximise the minimum distance between two points in the input space, and maximise the determinant of the matrix of covariance between the input factors (orthogonality constraint). In addition, the design excludes configurations with excessive eccentricity and unrealistic combinations of CO_2 and glaciation level.

- *Calibrate and validate and emulator.* The emulator is the Gaussian process emulator developed by Sacks et al. (1989), Kennedy and O'Hagan (2000) and Oakley and O'Hagan (2002). The validation was performed following a leave-one-out cross validation approach. Two experiments were excluded of the design as presenting an anomalous North-Atlantic convection pattern. The emulator calibrated on the remaining 59 experiments presents convincing validation scores.

- *Quantify and visualise the individual and combined effects of the different factors on summer Indian monsoon*, based on sensitivity indices and cross-section plots. This analysis yielded the following conclusions:

CPD
10, 1609–1651, 2014

Sensitivity analysis of Asian Monsoon

P. A. Araya-Melo et al.

- precession controls the response of four variables: continental temperature in phase with June–July insolation, high glaciation favouring a late-phase response, sea-surface temperature in phase with May insolation, and continental precipitation in phase with July insolation, and mixed-layer depth in antiphase with the latter.
- The effect CO_2 on continental temperature and SST is of similar size as that of precession on summer continental temperature and SST.
- Obliquity is a secondary effect, negligible on most variables except sea-surface temperature.
- The effect of glaciation is dominated by the albedo forcing, and its effect on precipitation competes with that of precession.
- The orographic forcing reduces the glacial cooling induced by the albedo forcing, and even has a positive effect on precipitation.

The originality of this study relies on the use of the *emulator* technique as a tool to provide reliable numerical results. We confirm that this technique has a large potential for the analysis of climate model outputs. Indeed, the study of any climatic event is far from straightforward when several variables are taken into account. In addition to state-of-the-art climate models, careful statistical modelling may significantly enhance to information that can be inferred from a well-chosen set of experiments. This holds regardless of the region of focus or the climate model being considered.

Acknowledgements. Paul Valdes and Gethin Williams are thanked for their assistance in setting up HadCM3 on our systems, and for providing us with ice topography boundary conditions. This research is a contribution to the ITOP project, ERC-StG grant 239604. MC is funded by the Belgian National Fund of Scientific Research (FRS-FNRS) and PA and NB are funded by the ERC ITOP project. Computational resources have been provided by the supercomputing facilities of the Université catholique de Louvain (CISM/UCL) and the Consortium des Equipements de Calcul Intensif en Fédération Wallonie Bruxelles (CECI) funded by the FRS-FNRS.

CPD
10, 1609–1651, 2014

References

Anderson, P. M., Barnosky, C. W., Bartlein, P. J., Behling, P. J., Brubaker, L., Cushing, E. J., Dodson, J., Dworetsky, B., Guetter, P. J., Harrison, S. P.,Huntley, B., Kutzbach, J. E., Markgraf, V., Marvel, R., McGlone, M. S., Mix, A., Moar, N. T., Morley, J., Perrott, R. A., Peterson, G. M., Prell, W. L., Prentice, I. C., Ritchie, J. C., Roberts, N., Ruddiman, W. F., Salinger, M. J., Spaulding, W. G., Street-Perrott, F. A., Thompson, R. S., Wang, P. K., Webb III, T., Winkler, M. G., and Wright Jr., H. E.: Climatic changes of the last 18,000 years – observations and model simulations, Science, 241, 1043–1052, doi:10.1126/science.241.4869.1043, 1988. 1611, 1612

Andrianakis, I. and Challenor, P. G.: The effect of the nugget on Gaussian process emulators of computer models, Comput. Stat. Data An., 56, 4215–4228, doi:10.1016/j.csda.2012.04.020, 2012. 1618, 1619

Bastos, L. S. and O'Hagan, A.: Diagnostics for Gaussian process emulators, Technometrics, 51, 425–438, doi:10.1198/TECH.2009.08019, 2009. 1618

Berger, A. L.: Long-term variations of daily insolation and Quaternary climatic changes, J. Atmos. Sci., 35, 2362–2367, doi:10.1175/1520-0469(1978)035<2362:LTVODI>2.0.CO;2, 1978. 1620

Berger, J. O., De Oliveira, V., and Sansó, B.: Objective Bayesian analysis of spatially correlated data, J. Am. Stat. Assoc., 96, 1361–1374, doi:10.1198/016214501753382282, 2001. 1618

Braconnot, P. and Marti, O.: Impact of precession on monsoon characteristics from coupled ocean atmosphere experiments: changes in Indian monsoon and Indian ocean climatology, Mar. Geol., 201, 23–34, doi:10.1016/S0025-3227(03)00206-8, asian Monsoons and Global Linkages on Milankovitch and Sub-Milankovitch Time Scales, 2003. 1611, 1612, 1627

Braconnot, P., Loutre, M., Dong, B., Joussaume, S., and Valdes, P.: How the simulated change in monsoon at 6 ka BP is related to the simulation of the modern climate: results from the Paleoclimate Modeling Intercomparison Project, Clim. Dynam., 19, 107–121, doi:10.1007/s00382-001-0217-5, 2002. 1611, 1612

Braconnot, P., Otto-Bliesner, B., Harrison, S., Joussaume, S., Peterchmitt, J.-Y., Abe-Ouchi, A., Crucifix, M., Driesschaert, E., Fichefet, Th., Hewitt, C. D., Kageyama, M., Kitoh, A., Laîné, A., Loutre, M.-F., Marti, O., Merkel, U., Ramstein, G., Valdes, P., Weber, S. L., Yu, Y., and Zhao, Y.: Results of PMIP2 coupled simulations of the Mid-Holocene and Last

Glacial Maximum – Part 1: experiments and large-scale features, Clim. Past, 3, 261–277, doi:10.5194/cp-3-261-2007, 2007. 1616

Braconnot, P., Marzin, C., Grégoire, L., Mosquet, E., and Marti, O.: Monsoon response to changes in Earth's orbital parameters: comparisons between simulations of the Eemian and of the Holocene, Clim. Past, 4, 281–294, doi:10.5194/cp-4-281-2008, 2008. 1611, 1613, 1626

Dong, B. W. and Valdes, P. J.: Modelling the Asian summer monsoon rainfall and Eurasian winter/spring snow mass, Q. J. Roy. Meteor. Soc., 124, 2567–2596, doi:10.1002/qj.49712455203, 1998. 1612

Essery, R. L. H., Best, M. J., Betts, R. A., Cox, P. M., and Taylor, C. M.: Explicit representation of subgrid heterogeneity in a GCM land-surface scheme, J. Hydrometeorol., 4, 530–543, doi:10.1175/1525-7541(2003)004<0530:EROSHI>2.0.CO;2, 2003. 1616

Felzer, B., Webb III, T., and Oglesby, R. J.: The impact of ice sheets, CO_2, and orbital insolation on late quaternary climates: sensitivity experiments with a general circulation model, Quaternary Sci. Rev., 17, 507–534, doi:10.1016/S0277-3791(98)00010-9, 1998. 1612

Gordon, C., Cooper, C., Senior, C. A., Banks, H., Gregory, J. M., Johns, T. C., Mitchell, J. F. B., and Wood, R. A.: The simulation of SST, sea ice extents and ocean heat transports in a version of the Hadley Centre coupled model without flux adjustments, Clim. Dynam., 16, 147–168, doi:10.1007/s003820050010, 2000. 1614, 1616

Gramacy, R. and Lee, H. H.: Cases for the nugget in modeling computer experiments, Stat. Comput., 22, 713–722, doi:10.1007/s11222-010-9224-x, 2012. 1619

Hewitt, C. D.: The effects of ocean dynamics in a coupled GCM simulation of the Last Glacial Maximum, Clim. Dynam., 20, 203–218, doi:10.1007/s00382-002-0272-6, 2003. 1624

Hewitt, C. D., Broccoli, A. J., Crucifix, M., Gregory, J. M., Mitchell, J. F. B., and Stouffer, R. J.: The effect of a large freshwater perturbation on the Glacial Atlantic Ocean using a coupled general circulation model, J. Climate, 19, 4436–4447, doi:10.1175/JCLI3867.1, 2006. 1624

Homma, T. and Saltelli, A.: Importance measures in global sensitivity analysis of nonlinear models, Reliab. Eng. Syst. Safe., 52, 1–17, doi:10.1016/0951-8320(96)00002-6, 1996. 1613, 1621

Joseph, V. R. and Hung, Y.: Orthogonal-maximin latin hypercube designs, Stat. Sinica, 18, 171–186, 2008. 1615

CPD

10, 1609–1651, 2014

Sensitivity analysis of Asian Monsoon

P. A. Araya-Melo et al.

Joussaume, S., Taylor, K. E., Braconnot, P., Mitchell, J. F. B., Kutzbach, J. E., Harrison, S. P., Prentice, I. C., Broccoli, A. J., Abe-Ouchi, A., Bartlein, P. J., Bonfils, C., Dong, B., Guiot, J., Herterich, K., Hewitt, C. D., Jolly, D., Kim, J. W., Kislov, A., Kitoh, A., Loutre, M. F., Masson, V., McAvaney, B., McFarlane, N., de Noblet, N., Peltier, W. R., Peterschmitt, J. Y., Pollard, D., Rind, D., Royer, J. F., Schlesinger, M. E., Syktus, J., Thompson, S., Valdes, P., Vettoretti, G., Webb, R. S., and Wyputta, U.: Monsoon changes for 6000 years ago: results of 18 simulations from the Paleoclimate Modeling Intercomparison Project (PMIP), Geophys. Res. Lett., 26, 859–862, doi:10.1029/1999GL900126, 1999. 1612

Kennedy, M. C. and O'Hagan, A.: Predicting the output from a complex computer code when fast approximations are available, Biometrika, 87, 1–13, doi:10.1093/biomet/87.1.1, 2000. 1617, 1619, 1630

Kutzbach, J. E. and Guetter, P. J.: The influence of changing orbital parameters and surface boundary conditions on climate simulations for the past 18 000 years, J. Atmos. Sci., 43, 1726–1759, doi:10.1175/1520-0469(1986)043<1726:TIOCOP>2.0.CO;2, 1986. 1611

Kutzbach, J. E. and Liu, Z.: Response of the African Monsoon to orbital forcing and ocean feedbacks in the middle Holocene, Science, 278, 440–443, doi:10.1126/science.278.5337.440, 1997. 1611, 1612

Kutzbach, J. E. and Ruddiman, W. F.: Model description, external forcing, and surface boundary conditions, in: Global climates since the last glacial maximum, 12–23, 1993. 1611

Kutzbach, J. E. and Street-Perrott, F. A.: Milankovitch forcing of fluctuations in the level of tropical lakes from 18 to 0 kyr BP, Nature, 317, 130–134, doi:10.1038/317130a0, 1985. 1611, 1612

Loeppky, J. L., Sacks, J., and Welch, W. J.: Choosing the sample size of a computer experiment: a practical guide, Technometrics, 51, 366–376, doi:10.1198/TECH.2009.08040, 2009. 1616

Loutre, M. F.: Paramètres orbitaux et cycles diurne et saisonnier des insolations, Ph.D. thesis, Université catholique de Louvain, Louvain-la-Neuve, Belgium, 1993. 1615

MacCalman, A. D.: Flexible space-filling designs for complex system simulations, Ph.D. thesis, Naval Postgraduate School, Monterey, California, US, available at: http://hdl.handle.net/10945/34701,last access: 29 March 2014, 2013. 1616

Masson, V., Braconnot, P., Jouzel, J., de Noblet, N., Cheddadi, R., and Marchal, O.: Simulation of intense monsoons under glacial conditions, Geophys. Res. Lett., 27, 1747–1750, doi:10.1029/1999GL006070, 2000. 1612

McKay, M. D., Beckman, R. J., and Conover, W. J.: A comparison of three methods for selecting values of input variables in the analysis of output from a computer code, Technometrics, 21, 239–245, doi:10.2307/1268522, 1979. 1615

Morris, M. D. and Mitchell, T. J.: Exploratory designs for computational experiments, J. Stat. Plan. Infer., 43, 381–402, doi:10.1016/0378-3758(94)00035-T, 1995. 1615

Oakley, J. and O'Hagan, A.: Bayesian inference for the uncertainty distribution of computer model outputs, Biometrika, 89, 769–784, doi:10.1093/biomet/89.4.769, 2002. 1617, 1618, 1630

Oakley, J. E. and O'Hagan, A.: Probabilistic sensitivity analysis of complex models: a Bayesian approach, J. Roy. Stat. Soc. B, 66, 751–769, doi:10.1111/j.1467-9868.2004.05304.x, 2004. 1610, 1613, 1619, 1620

O'Hagan, A.: Bayesian analysis of computer code outputs: a tutorial, Reliab. Eng. Syst. Safe., 91, 1290–1300, doi:10.1016/j.ress.2005.11.025, 2006. 1613

Pepelyshev, A.: The role of the nugget term in the Gaussian process method, in: mODa 9 – Advances in Model-Oriented Design and Analysis, 149–156, Springer, 2010. 1619

Petropoulos, G., Wooster, M. J., Carlson, T. N., Kennedy, M. C., and Scholze, M.: A global Bayesian sensitivity analysis of the 1d SimSphere soil–vegetation–atmospheric transfer (SVAT) model using Gaussian model emulation, Ecol. Model., 220, 2427–2440, doi:10.1016/j.ecolmodel.2009.06.006, 2009. 1613

Prell, W. L. and Kutzbach, J. E.: Monsoon variability over the past 150,000 years, J. Geophys. Res.-Atmos., 92, 8411–8425, doi:10.1029/JD092iD07p08411, 1987. 1611

Prell, W. L. and Kutzbach, J. E.: The impact of Tibet-Himalayan elevation on the sensitivity of the monsoon climate system to changes in solar radiation, in: Tectonic Uplift and Climate Change, edited by: Ruddiman, W. F., Plenum Press, New York, 1997. 1629

Sacks, J., Welch, W. J., Mitchell, T. J., and Wynn, H. P.: Design and analysis of computer experiments, Stat. Sci., 4, 409–423, doi:10.1214/ss/1177012413, 1989. 1613, 1617, 1630

Saltelli, A., Tarantola, S., Campolongo, F., and Ratto, M.: Sensitivity analysis in practice, John Wiley and Sons, Ltd, Thichester, W. Sussex, England, 2004. 1621

Singarayer, J. S. and Valdes, P. J.: High-latitude climate sensitivity to ice-sheet forcing over the last 120 kyr, Quaternary Sci. Rev., 29, 43–55, doi:10.1016/j.quascirev.2009.10.011, 2010. 1615, 1641

Urban, N. M. and Fricker, T. E.: A comparison of Latin hypercube and grid ensemble designs for the multivariate emulation of an Earth system model, Comput. Geosci., 36, 746–755, doi:10.1016/j.cageo.2009.11.004, 2010. 1615

Williams, K. D., Senior, C. A., and Mitchell, J. F. B.: Transient climate change in the Hadley Centre Models: the role of physical processes, J. Climate, 14, 2659–2674, doi:10.1175/1520-0442(2001)014<2659:TCCITH>2.0.CO;2, 2001. 1628

Yin, Q. Z., Berger, A., and Crucifix, M.: Individual and combined effects of ice sheets and precession on MIS-13 climate, Clim. Past, 5, 229–243, doi:10.5194/cp-5-229-2009, 2009. 1629

Zhao, Y., Braconnot, P., Marti, O., Harrison, S. P., Hewitt, C. D., Kitoh, A., Liu, Z., Mikolajewicz, U., Otto-Bliesner, B., and Weber, S. L.: A multi-model analysis of the role of the ocean on the African and Indian monsoon during the mid-Holocene, Clim. Dynam., 25, 777–800, doi:10.1007/s00382-005-0075-7, 2005. 1614, 1622, 1626, 1627

CPD

10, 1609–1651, 2014

Table 1. Experiment setup: simulation name and number, astronomical parameters (eccentricity, longitude of the perihelion and obliquity), CO_2 concentration and glaciation level.

#	Name	e –	ϖ (°)	ε (°)	CO_2 (ppm)	Ice level –	#	Name	e –	ϖ (°)	ε (°)	CO_2 (ppm)	Ice level –
1	xadba	0.0527	53.52	23.6	277.3	1	32	xadfa	0.0383	334.53	23.8	257.8	6
2	xadbb	0.0520	211.44	22.9	267.5	1	33	xadfb	0.0417	139.99	24.5	214.1	6
3	xadbc	0.0309	218.44	23.1	262.6	1	34	xadfc	0.0480	215.67	23.2	225.0	6
4	xadbd	0.0201	350.24	23.2	271.2	1	35	xadfd	0.0404	140.60	22.1	225.0	6
5	xadka	0.0282	256.84	24.2	264.1	2	36	xadga	0.0301	194.43	22.4	254.1	7
6	xadkb	0.0466	228.06	24.2	263.4	2	37	xadgb	0.0261	208.55	22.9	189.8	7
7	xadkc	0.0411	88.21	23.3	273.5	2	38	xadgc	0.0503	202.65	24.3	260.8	7
8	xadkd	0.0077	358.66	22.3	255.1	2	39	xadgd	0.0389	122.16	22.3	257.8	7
9	xadaa	0.0403	316.14	22.1	270.6	3	40	xadge	0.0345	97.90	23.4	246.8	7
10	xadab	0.0263	271.85	22.2	270.7	3	41	xadgf	0.0362	299.18	22.2	246.8	7
11	xadac	0.0416	140.71	22.7	269.6	3	42	xadgg	0.0440	355.96	24.0	260.9	7
12	xadad	0.0257	167.54	22.6	256.1	3	43	xadgh	0.0422	287.83	24.7	203.2	7
13	xadae	0.0406	167.95	23.1	240.7	3	44	xadha	0.0436	51.20	22.5	192.6	8
14	xadaf	0.0460	305.89	23.9	224.9	3	45	xadhb	0.0333	26.49	22.7	254.3	8
15	xadag	0.0293	93.07	22.3	264.7	3	46	xadhc	0.0461	205.77	24.3	186.2	8
16	xadda	0.0244	323.78	22.8	214.1	4	47	xadhd	0.0386	246.02	23.1	214.1	8
17	xaddb	0.0421	114.71	23.7	214.2	4	48	xadhe	0.0405	38.22	24.8	225.0	8
18	xaddc	0.0253	23.96	23.6	235.9	4	49	xadhf	0.0491	221.00	23.6	235.9	8
19	xaddd	0.0469	1.20	24.9	235.1	4	50	xadia	0.0150	341.91	22.8	244.4	9
20	xadei	0.0000	0.00	23.0	230.4	5	51	xadib	0.0457	78.40	23.0	235.9	9
21	xadej	0.0500	90.00	23.0	230.4	5	52	xadic	0.0226	113.92	23.0	225.0	9
22	xadek	0.0500	0.00	23.0	230.4	5	53	xadid	0.0400	53.05	22.4	232.9	9
23	xadel	0.0000	0.00	24.0	230.4	5	54	xadie	0.0336	143.57	24.9	231.3	9
24	xadea	0.0155	217.23	23.4	205.9	5	55	xadja	0.0452	260.43	24.0	182.0	10
25	xadeb	0.0527	52.54	24.2	235.9	5	56	xadjb	0.0444	319.59	24.4	209.2	10
26	xadec	0.0456	4.52	24.1	206.6	5	57	xadjc	0.0463	192.48	24.7	191.0	10
27	xaded	0.0135	68.81	24.6	246.8	5	58	xadca	0.0350	305.63	24.1	190.5	11
28	xadee	0.0236	260.39	24.5	217.6	5	59	xadcb	0.0137	145.99	23.9	216.4	11
29	xadef	0.0396	285.78	25.0	246.8	5	60	xadcc	0.0250	136.64	23.3	186.4	11
30	xadeg	0.0251	276.28	24.3	271.0	5	61	xadcd	0.0243	75.55	22.9	197.7	11
31	xadeh	0.0404	359.97	23.5	206.9	5							

CPD
10, 1609–1651, 2014
Sensitivity analysis of Asian Monsoon
P. A. Araya-Melo et al.

Table 2. Emulator scales for the different fields under study., In general, scales are commesurate with the range covered by the input factors. However, for CO_2 and sometimes obliquity, the scales are much larger than the fields' scale. This just indicates that the response is linear with respect to the factor.

	Lambda					Nugget
	$\lambda_{e\cos\varpi}$ –	$\lambda_{e\sin\varpi}$ –	λ_{ε} (°)	λ_{CO_2} (ppm)	λ_{ice} –	
Land temperature	0.0704	0.0914	1.595	935	3.348	0.0047
Land precipitation	0.1153	0.3037	10.11	12 520	2.2807	0.0188
Sea surface temperature	0.1118	0.1142	300.	9732	7.307	0.0035
Mixed-layer depth	0.0767	0.0308	1.886	409	10.6960	0.0439

CPD
10, 1609–1651, 2014

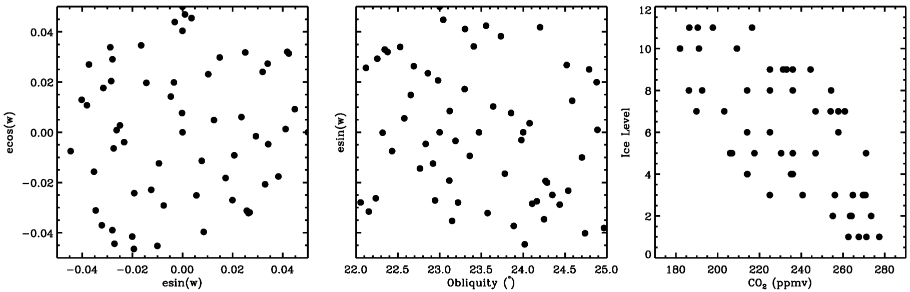

Fig. 1. Experiment plan design, optimised to order to maximize the minimum distance between points and to achieve orthogonality (maximise the determinant of the covariance of input factors). Right: $e\cos\varpi$–$e\sin\varpi$ space distribution; middle: $e\sin\varpi$–obliquity space distribution; right: glaciation level–CO_2 space distribution.

CPD
10, 1609–1651, 2014

Sensitivity analysis of Asian Monsoon

P. A. Araya-Melo et al.

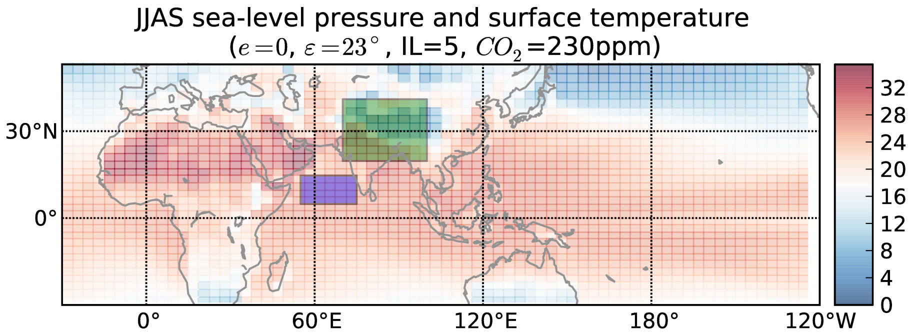

Fig. 2. JJAS sea-level pressure and surface temperature of the two regions depicted: NI and IND.

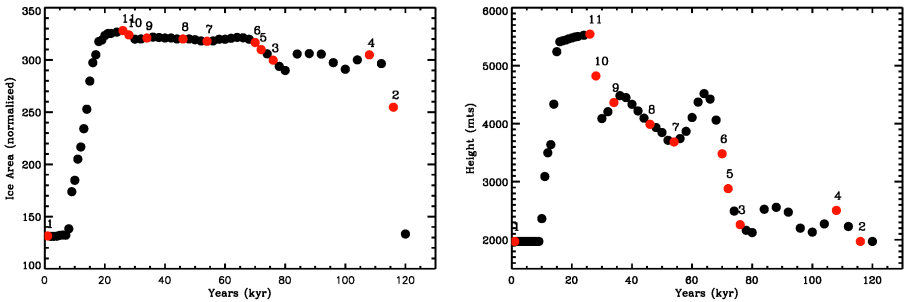

Fig. 3. Left panel: ice area, in normalized units, and maximum height (in meters) in the region 45–75° N and 240–275° W (Laurentide Ice Sheet), as a function of time in the boundary conditions used in the Singarayer and Valdes (2010) experiment. Red circles indicate the boundary conditions used for this specific study.

CPD
10, 1609–1651, 2014

Sensitivity analysis of Asian Monsoon

P. A. Araya-Melo et al.

Title Page
Abstract Introduction
Conclusions References
Tables Figures
◀ ▶
Back Close
Full Screen / Esc
Printer-friendly Version
Interactive Discussion

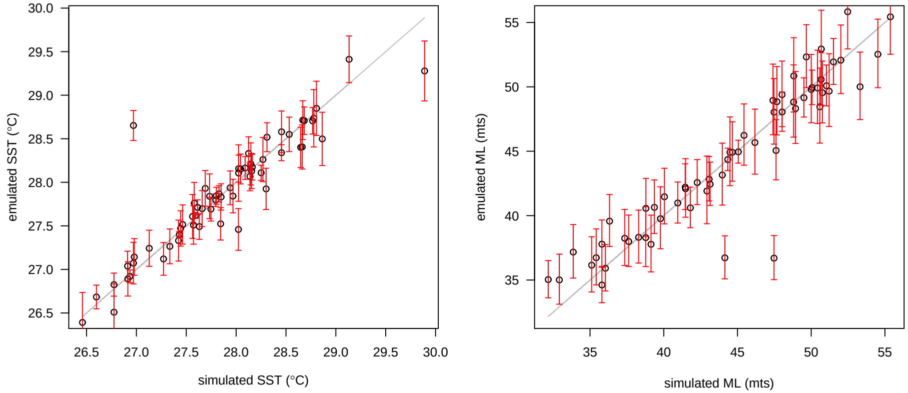

Fig. 4. Diagnostic of emulator performance considering experiments 11 and 40. Shown are the mean and standard deviations of sea surface temperature (left panel) and mixed-layer depth (right panel). Clearly seen are the two outliers, specially in the case of sea surface temperature.

CPD
10, 1609–1651, 2014

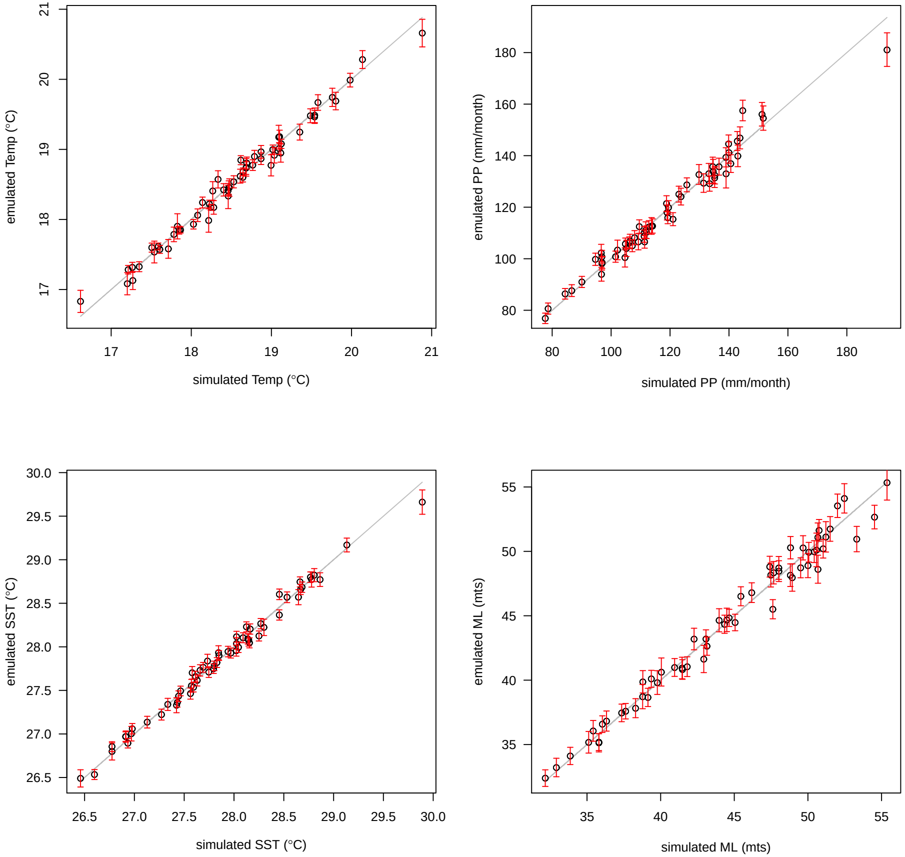

Fig. 5. Diagnostic of emulator performance. Shown are the mean and standard deviation of the simulated and the emulated data points for the all the simulations with the exception of simulation number 11 and 40. Top left panel: continental temperature; top right panel: continental precipitation; bottom left panel: sea surface temperature; bottom right panel: mixed layer depth.

CPD
10, 1609–1651, 2014

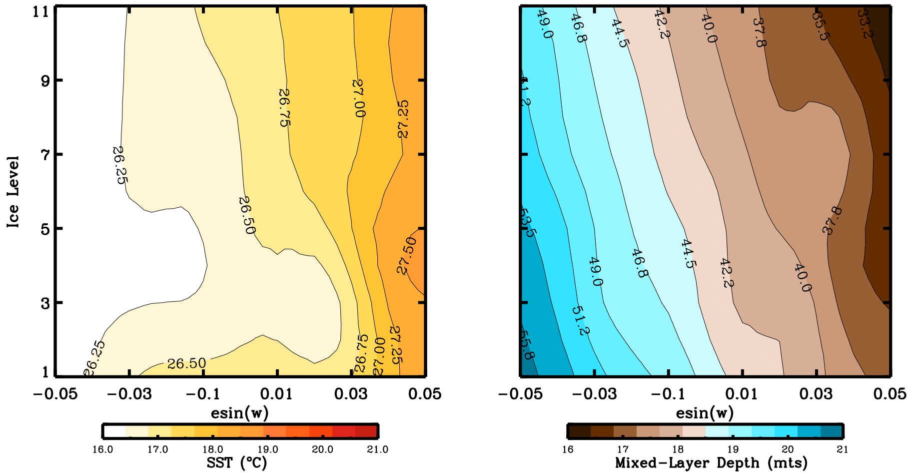

Fig. 6. Sensitivity to glaciation level and $e \sin\varpi$ for sea surface temperature and mixed-layer depth. The contour plots include the experiments 11 and 40. The effects of the outliers is clearly visible in both cases, ice level 3 in the case of sea surface temperature and glaciation level 7 for mixed-layer depth.

CPD
10, 1609–1651, 2014

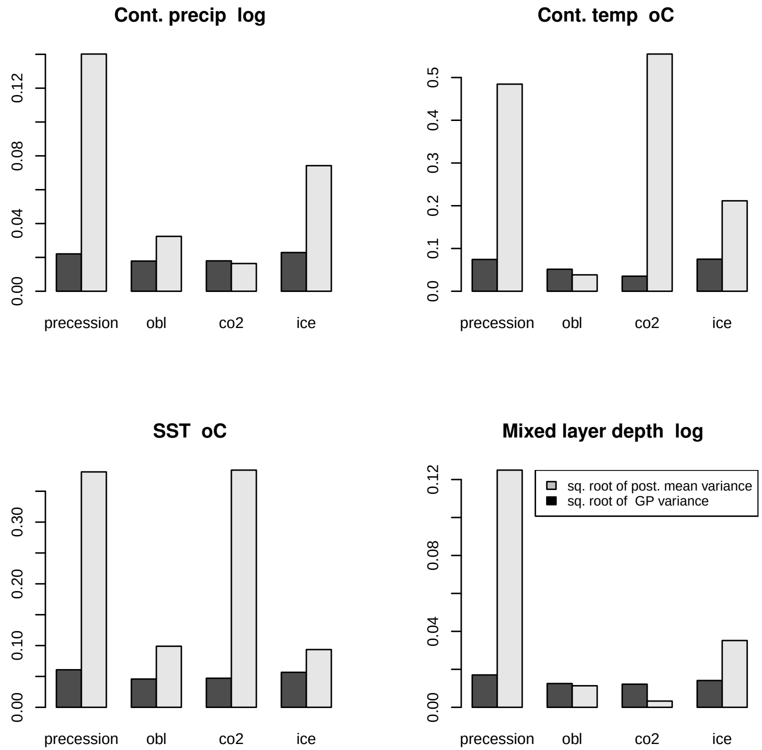

Fig. 7. Sensitivity analysis: shown is the standard deviation of model outputs ($\sqrt{S}$) of each variable, induced by variations in input factors during the Pleistocene. From left to right, top to bottom: continental precipitation, continental temperature, sea surface temperature and mixed-layer depth. The variance is partitioned between the effects associated with the response to output changes (grey) and Gaussian process variance (black), associated with using an emulator rather than direct simulator output.

CPD
10, 1609–1651, 2014

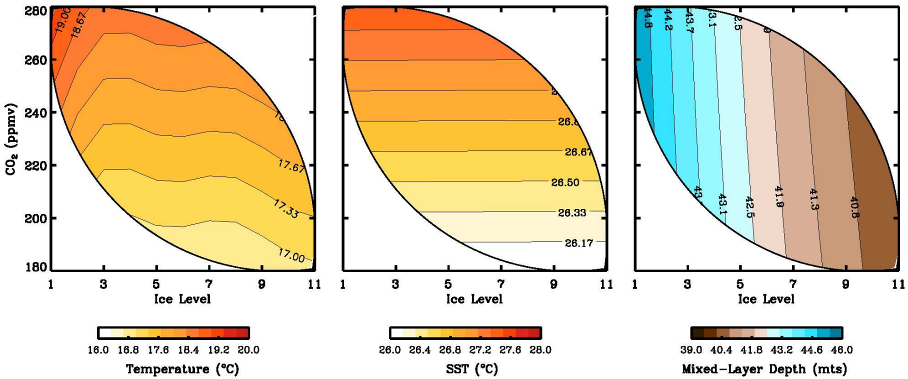

Fig. 8. Sensitivity to CO_2 and glaciation level. From left to right: continental temperature, sea surface temperature and mixed-layer depth. Fields were integrated over $e\sin(\varpi)$, $e\cos(\varpi)$ and obliquity.

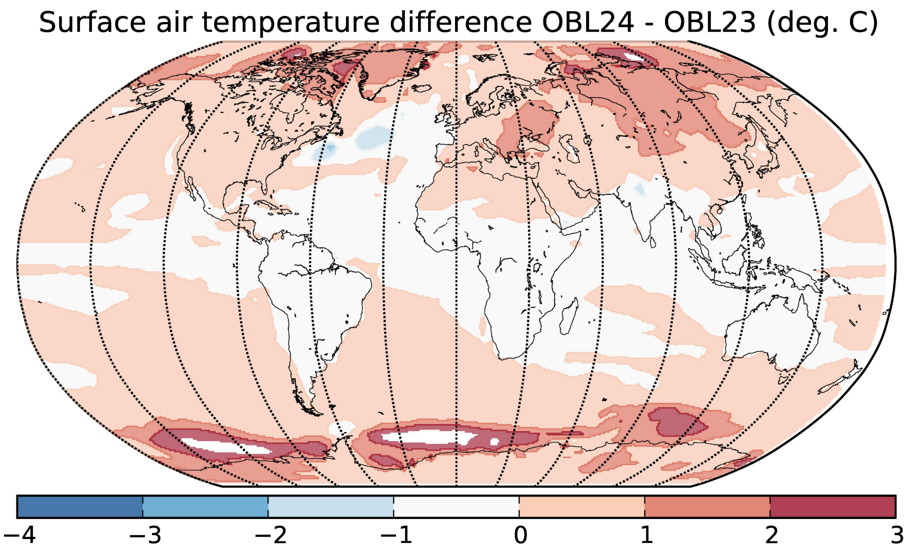

Fig. 9. Sea surface temperature difference for two *ideal* simulations. CO_2 concentration, glaciation level and precession remained fixed, the only difference being obliquity (23 and 24°).

CPD
10, 1609–1651, 2014

Sensitivity analysis of Asian Monsoon

P. A. Araya-Melo et al.

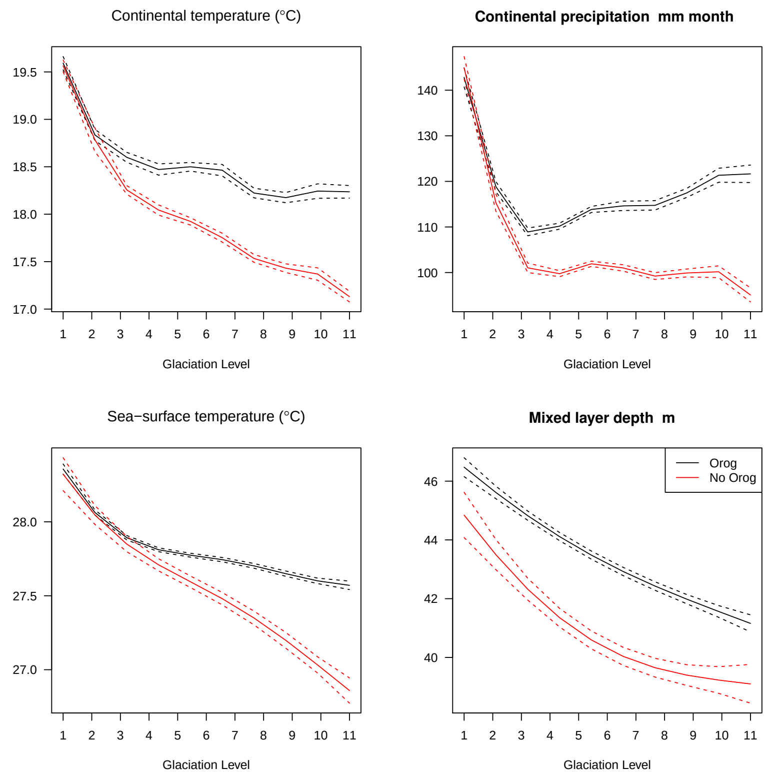

Fig. 10. Orography–no orography difference. From top to bottom, left to right: effect on continental temperature, precipitation, sea-surface temperature, and mixed-layer depth, with orography forcing (black) and without (red). The dotted lines show one standard deviation of the emulator prediction. One may see a departure point from glaciation level 3 in all four fields, as this is at this point that orography forcing becomes the most significant.

CPD
10, 1609–1651, 2014

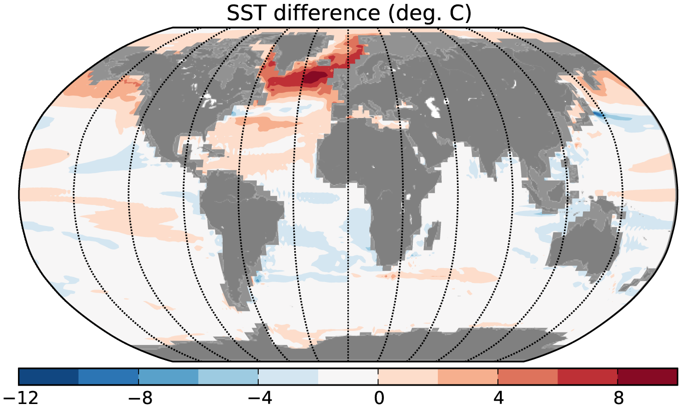

Fig. 11. Shown is the sea surface temperature difference between simulations 11 and 15 (see Table 1). There is a clear warming pattern in the North Atlantic, which affects the mean sea surface temperature.

CPD
10, 1609–1651, 2014

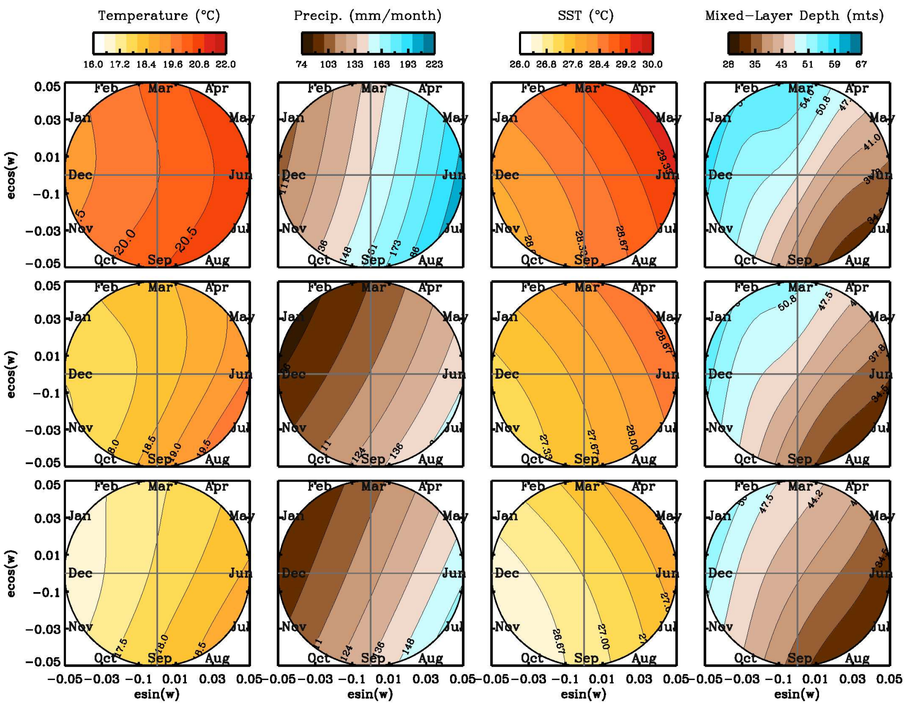

Fig. 12. Sensitivity to $e\cos(\varpi)$ and $e\sin(\varpi)$ for all fields. Each panel, from top to bottom, shows the four fields with a different configuration of glaciation level – CO_2 concentration. Top panels: glaciation level = 1 and CO_2 = 280 ppmv. Middle panels: glaciation level = 5 and CO_2 = 230. Bottom panels: glaciation level = 11 and CO_2 = 180. All fields were integrated over obliquity.

CPD
10, 1609–1651, 2014

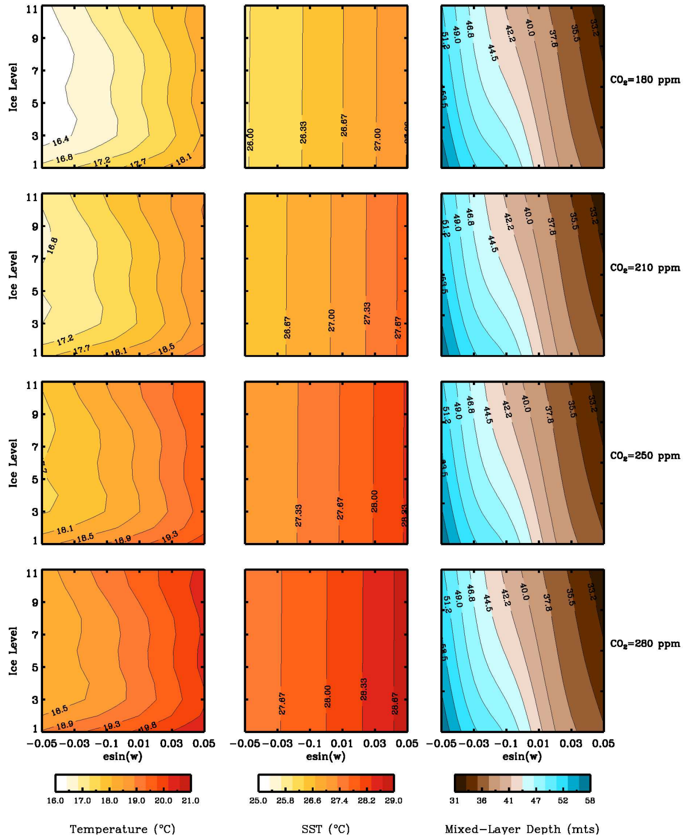

Fig. 13. Sensitivity to glaciation level and $e\sin(\varpi)$. Top left panel: temperature over NI; top right panel: precipitation over NI; bottom left panel: SST over IND; bottom right panel: mixed-layer depth over IND. The plots correspond to three different CO_2 concentrations: 180, 230 and 280 ppmv. All fields were integrated over obliquity and $e\cos(\varpi)$.

CPD
10, 1609–1651, 2014

Sensitivity analysis of Asian Monsoon

P. A. Araya-Melo et al.

Title Page
Abstract | Introduction
Conclusions | References
Tables | Figures
◀| |▶
◀ ▶
Back | Close
Full Screen / Esc
Printer-friendly Version
Interactive Discussion